CrossMark

RESEARCH ARTICLE

Krypton tagging velocimetry in a turbulent Mach 2.7 boundary layer

D. Zahradka[1] · N. J. Parziale[1] · M. S. Smith[2] · E. C. Marineau[2]

Abstract The krypton tagging velocimetry (KTV) technique is applied to the turbulent boundary layer on the wall of the "Mach 3 Calibration Tunnel" at Arnold Engineering Development Complex (AEDC) White Oak. Profiles of velocity were measured with KTV and Pitot-pressure probes in the Mach 2.7 turbulent boundary layer comprised of 99 % N_2/1 % Kr at momentum-thickness Reynolds numbers of $Re_\Theta = 800, 1400$, and 2400. Agreement between the KTV- and Pitot-derived velocity profiles is excellent. The KTV and Pitot velocity data follow the law of the wall in the logarithmic region with application of the Van Driest I transformation. The velocity data are analyzed in the outer region of the boundary layer with the law of the wake and a velocity-defect law. KTV-derived streamwise velocity fluctuation measurements are reported and are consistent with data from the literature. To enable near-wall measurement with KTV ($y/\delta \approx 0.1$–0.2), an 800-nm longpass filter was used to block the 760.2-nm read-laser pulse. With the longpass filter, the 819.0-nm emission from the re-excited Kr can be imaged to track the displacement of the metastable tracer without imaging the reflection and scatter from the read-laser off of solid surfaces. To operate the Mach 3 AEDC Calibration Tunnel at several discrete unit Reynolds numbers, a modification was required and is described herein.

✉ N. J. Parziale
nick.parziale@gmail.com

[1] Stevens Institute of Technology, 1 Castle Point on Hudson, Hoboken, NJ 07030-5991, USA

[2] AEDC White Oak, 10905 New Hampshire Avenue, Silver Spring, MD 20903, USA

1 Introduction

The need to accurately assess the heat transfer, skin friction, and velocity profiles on high-speed vehicles is born out of a thrust for rapid space access (Bilardo et al. 2003) and conventional prompt global strike (CPGS) (Woolf 2014). Progress has been made in the computation of high-speed and reacting flows, as reviewed in Candler (2015) and Schwartzentruber and Boyd (2015). Moreover, the uncertainty that arises from the application of the state-of-the-art (SOA) research codes to hypersonic problems has been characterized, as in Bose et al. (2013). Obtaining test and evaluation (T&E) data for high-speed vehicle development (Marren et al. 2001) and validation data for SOA research codes is the motivation for the development of new velocimetry diagnostics, especially for application in demanding testing environments.

There are a number of methodologies for making velocity measurements in fluid flows such as pressure-based measurement, thermal anemometry, and particle-based techniques (laser-Doppler velocimetry, global Doppler velocimetry, and particle image velocimetry (PIV)); for a contextual review see McKeon et al. (2007). The measurement of velocity with pressure-based and thermal anemometry methods are refined in that they can consistently yield data with low uncertainty; however, these techniques are intrusive, which eliminates them as candidates in certain flow regimes. Moreover, frequency response, spatial resolution, and required assumptions regarding the local temperature are limitations for velocity measurement using Pitot probes. Particle-based methods of velocimetry, PIV in particular, can currently produce high-quality multi-component velocity data (Clemens and Narayanaswamy 2014); in addition, PIV can yield field information about vorticity and pressure after further data processing (Charonko

et al. 2010). However, the limitations of implementing particle-based techniques in high-speed facilities include timing issues associated with particle injection (Haertig et al. 2002) and reduced particle response at Knudsen and Reynolds numbers (Loth 2008) typical of high-speed windtunnels.

An alternative velocimetry technique, tagging velocimetry, will be the focus of this paper; it is typically performed in gases by tracking the fluorescence of a native, seeded, or synthesized gas. In contrast to PIV, seeding and particle response issues are reduced or eliminated. Noted methods and tracers for tagging velocimetry include VENOM (Hsu et al. 2009a, b; Sánchez-González et al. 2011, 2012, 2014), APART (Dam et al. 2001; Sijtsema et al. 2002; Van der Laan et al. 2003), RELIEF (Miles et al. 1987, 1989, 1993, 2000; Miles and Lempert 1997), FLEET (Michael et al. 2011; Edwards et al. 2015), iodine (McDaniel et al. 1983; Balla 2013), acetone (Lempert et al. 2002, 2003; Handa et al. 2014), and the hydroxyl group (Boedeker 1989; Wehrmeyer et al. 1999; Pitz et al. 2005) among others (Hiller et al. 1984; Gendrich and Koochesfahani 1996; Gendrich et al. 1997; Stier and Koochesfahani 1999).

In this paper, we present the KTV setup and excitation/emission scheme which enables imaging the displaced Kr tracer at a different wavelength than that used to re-excite the Kr tracer. We describe a modification of the Mach 3 AEDC Calibration Tunnel which facilitates operation at several discrete unit Reynolds numbers consistent with AEDC Hypervelocity Tunnel 9 run conditions that are relevant to the study of shock-wave boundary layer interaction (SWBLI). We present KTV and Pitot probe-based velocity measurements for a Mach 2.7 turbulent boundary layer on a windtunnel wall. We non-dimensionalize the velocimetry results in the logarithmic and outer regions of the boundary layer, and we present fluctuation data derived from KTV measurements and compare it to data from the literature.

2 Krypton tagging velocimetry (KTV) setup

Krypton tagging velocimetry (KTV), relative to other tagging velocimetry techniques, relies on a chemically inert tracer. This property may enable KTV to broaden the utility of tagging velocimetry because the technique can be applied in gas flows where the chemical composition is difficult to prescribe or predict. The use of a metastable noble gas as a tagging velocimetry tracer was first suggested by Mills et al. (2011) and Balla and Everhart (2012). KTV was first demonstrated by Parziale et al. (2015a, b) to measure the velocity along the centerline of an underexpanded jet of N_2/Kr mixtures. In that work, pulsed tunable lasers were used to induce fluorescence of Kr atoms that were seeded into the flow for the purposes of displacement tracking.

The excitation/emission scheme used in this work is slightly different than in the original KTV work by Parziale et al. (2015a, b). Two high-precision 800-nm longpass filters (Thorlabs FELH0800, transmission of 5e−4 % at the read-laser wavelength of 760.2 nm) are placed in series in front of the image intensifier to minimize the noise resulting from the read-laser pulse reflection and scatter from solid surfaces. This was done to enable the imaging of fluorescing Kr atoms near the windtunnel wall.

Following the energy level diagram (Racah nl[K]$_J$ notation) in Fig. 1, KTV is performed as follows:

1. Seed a base flow with krypton locally or globally.
2. Photosynthesize metastable krypton atoms with a pulsed tunable laser to form the tagged tracer: two-photon excitation of $4p^6(^1S_0) \rightarrow 5p[3/2]_2$ (214.7 nm) and rapid decay to $5p[3/2]_2 \rightarrow 5s[3/2]_1^o$ (819.0 nm) and the metastable state via $5p[3/2]_2 \rightarrow 5s[3/2]_2^o$ (760.2 nm). We estimate that the creation of the metastable atoms which comprise the "write line," or tracer, takes approximately 50 ns (Chang et al. 1980).
3. Record the displacement of the tagged metastable krypton by imaging the laser induced fluorescence (LIF) that is produced with an additional pulsed tunable laser: re-excite $5p[3/2]_2$ level by $5s[3/2]_2^o \rightarrow 5p[3/2]_2$ transition with laser sheet (760.2 nm) and read spontaneous emission of $5p[3/2]_2 \rightarrow 5s[3/2]_1^o$ (819.0 nm) transitions with a camera positioned normal to the flow. We estimate that the fluorescence from the Kr tracer occurs approximately 50 ns after the read-laser pulse.

The experiment was run using two tunable lasers to provide the 214.7 nm (write) and 760.2 nm (read) laser beams required for KTV (schematic in Fig. 2). The write-laser consisted of a frequency tripled PR8010 Nd:YAG laser and a frequency doubled Continuum ND6000 Dye Laser. The Nd:YAG laser pumped the dye laser with 400 mJ/pulse at a wavelength of 355 nm. The dye in the laser was
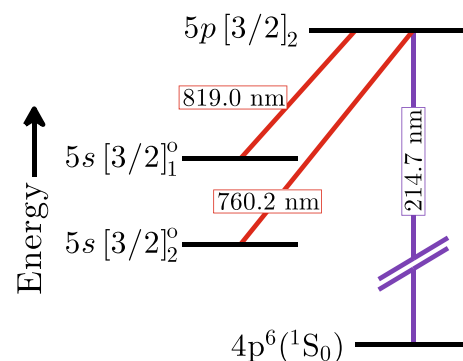

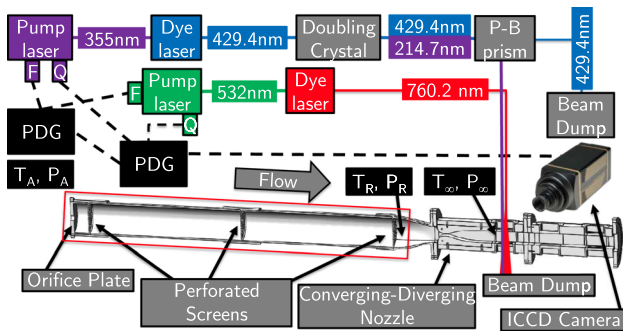**Fig. 1** Energy diagram for KTV. Racah nl[K]$_J$ notation

Fig. 2 Setup of experiment with lasers, test section, and tunnel modification (*boxed* in *red*). *F* flashlamp, *Q* Q-switch, *PDG* pulse delay generator, *P–B* prism is Pellin–Broca prism

Coumarin 440 and the laser was tuned to output a 429.4 nm beam. Frequency doubling of the dye laser output was preformed using an Inrad BBO-C (65°) crystal placed in a Inrad 820-360 gimbal mount, resulting in a laser beam with two wavelengths, 214.7 and 429.4 nm. The 214.7 and 429.4 nm beams were separated with a Pellin–Broca prism. The 429.4 nm wavelength beam was sent to a beam dump and the 214.7 nm wavelength beam was directed to the test section.

The write-laser beam setup resulted in approximately 1 mJ/pulse, with a wavelength of 214.7 nm, a linewidth of approximately 0.3 cm^{-1}, a pulsewidth of approximately 7 ns, and a repetition rate of 10 Hz. The write-laser beam was directed into the test section with 1 in. fifth-harmonic Nd:YAG laser mirrors (IDEX Y5-1025-45) and focused to a narrow waist into the test section with a 1000-mm fused-silica lens. The full width at half maximum (FWHM) of the beam intensity profile is observed to be ≈350 μm (Fig. 6) and the peak beam fluence was ≈500 mJ/cm^2. This narrow laser beam photosynthesizes the metastable krypton atoms that comprise the tracer forming the "write line".

The read-laser consisted of a frequency doubled Continuum NY82S-10 Nd:YAG laser and a Continuum ND60 Dye Laser. The Nd:YAG laser pumped the dye laser with

250 mJ/pulse at a wavelength of 532 nm. The dye in the laser was LDS 765 and the laser was tuned to output a 760.15 nm beam.

The read-laser beam setup resulted in approximately 20 mJ/pulse, with a wavelength of 760.15 nm, a linewidth of approximately 0.3 cm^{-1}, a pulsewidth of approximately 8 ns, and a repetition rate of 10 Hz. The read-laser beam was directed into the test section using 2 in. broadband dielectric mirrors (Thorlabs BB2-E02) as a sheet of ≈200 μm thickness. This "read sheet" re-excites the metastable Kr tracer atoms so that their displacement can be measured.

The laser and camera timing is controlled by pulse delay generators (SRS DG535). The intensified camera used for all experiments is a 16-bit Princeton Instruments PIMAX-2 1024 × 1024 with an 18 mm Gen III Unigen intensifier. The gain is set to 255 with 2 × 2 pixel binning to ensure a 10-Hz frame rate. The camera gate was opened for 50 ns to bracket the read-laser pulse to capture the spontaneous emission of $5p[3/2]_2 \rightarrow 5s[3/2]_1^o$ (819.0 nm) transitions.

The KTV and Pitot probe measurements are made ≈530 and ≈280 mm from the nozzle throat and nozzle exit, respectively; this is the location of the "Port 2" in the test section (Figs. 2, 3). The write- and read-laser beams pass through UV fused-silica windows to enter and leave the test section. The UV fused-silica windows were undamaged by the laser pulses so long as the window surface was kept clean. To avoid damage, lens tissue was used to remove dirt and oil every ten experiments.

3 Mach 3 AEDC calibration tunnel and modification

The purpose of conducting KTV experiments in the Mach 3 AEDC Calibration Tunnel was to demonstrate that the technique could be utilized in AEDC Hypervelocity Tunnel 9, which is a large-scale N_2 blow-down hypersonic windtunnel (Marren and Lafferty 2002). The Mach 3 AEDC Calibration Tunnel is a large vacuum tank with a
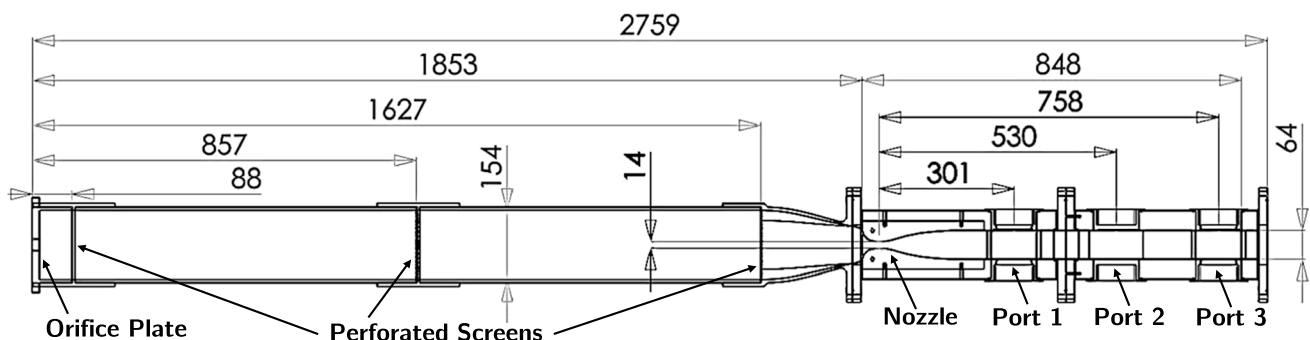

Fig. 3 Sketch of AEDC Mach 3 calibration tunnel. Dimensions in millimeters. The KTV and Pitot measurements are made at "Port 2"

converging-diverging nozzle attached to it. To start the tunnel, a valve is cycled downstream of the nozzle throat. The effective reservoir is the ambient laboratory air and so the freestream conditions are fixed.

In its original configuration, the Mach 3 AEDC Calibration Tunnel and AEDC Tunnel 9 operate with different run conditions; that is, AEDC Tunnel 9 typically operates with a lower freestream pressure than does the Mach 3 AEDC Calibration Tunnel. This has implications on the SNR of the KTV technique because of the population available for fluorescence (Eckbreth 1996) and the quenching of the metastable Kr tracer (Velazco et al. 1978).

To account for the difference in pressure, modifications were made to the tunnel upstream of the nozzle (boxed in red in Fig. 2 and to the left of the nozzle in Fig. 3). The effective reservoir pressure was reduced by choking the flow upstream of the throat with an orifice plate. A PVC pipe housed perforated screens that were used to breakup the jet from the orifice plate which was a PVC end cap with a hole drilled in it. Three caps with holes of diameter 12.7, 19.1, and 25.4 mm were used to alter the mass flow rate, and thus, the effective pressure drop.

To estimate the reduced reservoir pressure, choked flow calculations were used where sonic flow was assumed at the orifice plate and nozzle throat. The mass flow rate of the gas into the tube from the ambient lab to the effective reservoir was determined using

$$\dot{m} = C_{OP} A_{OP} \sqrt{\gamma \rho_A P_A \left(\frac{2}{\gamma + 1} \right)^{\frac{\gamma+1}{\gamma-1}}} \qquad (1)$$

and then the mass flow rate of the gas into the tube from effective reservoir to the freestream was determined using

$$\dot{m} = C_{noz} A_{noz} \sqrt{\gamma \rho_R P_R \left(\frac{2}{\gamma + 1} \right)^{\frac{\gamma+1}{\gamma-1}}} \qquad (2)$$

where the subscripts "OP" and "noz" refer to the orifice plate and the nozzle, respectively. We assume that the flow is steady so that the mass flow rates in Eqs. 1 and 2 must match. Furthermore, we assume that the discharge coefficients, C_{OP} and C_{noz} are unity and that there are no standing shock waves within the tube (no change in total pressure). Equating Eqs. 1 and 2 and solving for P_R results in

$$P_R = P_A \sqrt{\frac{T_R}{T_A}} \frac{A_{OP}}{A_{noz}}. \qquad (3)$$

We found that the effective reservoir pressure could be reduced by a factor of approximately 2, 4, and 10 for the 25.4, 19.1, and 12.7 mm orifice plates, respectively. Predicted freestream static pressure values from Eq. 3 for the 25.4, 19.1, and 12.7 mm orifice plates are 1920, 1080, and

480 Pa, respectively; these predicted static pressures are within 10 % of the measured static pressures in Table 1. This method is a promising strategy for controlling the Reynolds number of the flow in the Mach 3 AEDC Calibration Tunnel.

An isolation bag was added to the end of the tube over the orifice plate which isobarically isolates the test gas from the ambient air in the laboratory. The bag is flexible, so the test gas in the isolation bag is at constant ambient pressure throughout an experiment. The test section, PVC tube, and isolation bag could be filled with high-purity mixtures of nitrogen and krypton.

The run conditions with each of the orifice plates were calculated by measuring the static pressure, P_∞, and Pitot pressure, P_{02}, with Micro Switch 130PC pressure transducers [details are given in Section II of Brooks et al. (2015)], and finding the freestream Mach number with the Rayleigh–Pitot probe formula (Liepmann and Roshko 1957), which is written as

$$\frac{P_{02}}{P_\infty} = \left(\frac{(\gamma + 1)^2 M_\infty^2}{4\gamma M_\infty^2 - 2(\gamma - 1)} \right)^{\left(\frac{\gamma}{\gamma-1} \right)}$$
$$\times \left(\frac{1 - \gamma + 2\gamma M_\infty^2}{\gamma + 1} \right). \qquad (4)$$

The freestream temperature (and thus freestream velocity) were found by assuming isentropic expansion as

$$T_\infty = T_R \left(1 + \frac{\gamma - 1}{2} M_\infty^2 \right)^{-1}. \qquad (5)$$

It was determined by Omega 5TC-TT-E-40-36 thermocouple measurement that the reservoir temperature and ambient temperature are approximately equal; that is, $T_R = T_A$ in Fig. 2. Freestream conditions for each orifice plate are listed in Table 1. Example measurements for the static pressure, Pitot pressure, and reservoir temperature are presented in Fig. 4. The expansion wave that propagates through the PVC tube during tunnel startup can be seen between 0.75–2.0 s. The steady test time is approximately 3 s, between 2 and 5 s.

4 Effect of run condition on metastable lifetime

The SNR of a fluorescence technique is proportional to the local number density of the fluorescing constituent (Eckbreth 1996). However, in the case of KTV, increasing the local number density also increases the decay rate of the photosynthesized metastable Kr $5s[3/2]_2^o$ tracer (Velazco et al. 1978). This presents the researcher with the task of maximizing the SNR by balancing the local number density with the decay rate of the tracer. In this section, we present

Table 1 $M_\infty, P_\infty, T_\infty, \rho_\infty, Re_\infty^{unit}, Re_\Theta$, and U_∞ are the Mach number, pressure, temperature, density, unit Reynolds number, momentum-thickness Reynolds number, and velocity for each experiment. τ_m and x_m are the calculated time and distance scale, respectively, for the decay of the metastable Kr state. $M_\tau, B_q, 2\Pi/\kappa$, and δ are the turbulence Mach number, heat flux number, wake-strength parameter, and boundary layer thickness, respectively

Experiment	M_∞ (–)	P_∞ (Pa)	T_∞ (K)	ρ_∞ (kg/m³)	Re_∞^{unit} (1/m)	Re_Θ (–)	U_∞ (mm/μs)	$10\tau_m$ (μs)	x_m (mm)	M_τ (–)	B_q (–)	$2\Pi/\kappa$ (–)	δ (mm)
Underexpanded Jet	5.00	340	49.3	0.024	79.7e6	–	0.714	4.5	3.2	–	–	–	–
M3 AEDC—12.7 mm OP	2.75	550	118	0.016	1.26e6	800	0.614	7.6	4.7	0.107	0.0053	0.73	12.0
M3 AEDC—19.1 mm OP	2.77	1010	118	0.030	2.30e6	1400	0.612	4.1	2.5	0.099	0.0049	1.18	10.4
M3 AEDC—25.4 mm OP	2.73	1825	118	0.053	4.16e6	2400	0.611	2.1	1.4	0.093	0.0046	1.42	9.7
AEDC Tunnel 9 Run 3742	9.86	600	53.4	0.038	15.0e6	–	1.469	3.15	4.6	–	–	–	–
Caltech T5 Shot 2773	5.93	6000	1014	0.020	1.80e6	–	3.860	5.98	23	–	–	–	–

estimates of the relevant figures pertaining to the de-excitation rate of the metastable Kr tracer for flows of interest.

Velazco et al. (1978) tabulate the quenching rate constants of the $5s[3/2]_2^o$ state with a number of collisional partners of interest in the aerothermodynamics and combustion communities. Using the plug flow approximation, they used a flow reactor to determine the timescale of metastable state decay as

$$\frac{1}{\tau_m} = \frac{D_0}{\Lambda^2 P} + k_1 P + k_2 P + k_Q[Q], \tag{6}$$

where the first three terms are due to diffusion, and two-body and three-body de-excitation processes in the argon carrier gas, respectively. The fourth term, $k_Q[Q]$ is the timescale associated with the de-excitation of the metastable state with an added reagent; this is the rate which will dominate the de-excitation of metastable Kr atoms in typical fluid mechanics applications.

If we assume a fluorescence signal towards the high side of the 16-bit camera's dynamic range at the write location (which has been demonstrated with the current experimental setup), then the number of recordable metastable lifetimes is estimated as $2^{16} \approx \exp(-t/\tau_m)$. We take $\ln(2^{16}) \approx 10 = t/\tau_m$ which leads to the estimation that we can record the displacement of metastable Kr for approximately ten lifetimes.

In Table 1, we list the relevant parameters for KTV measurement; namely, local density, ρ_∞, and the length scale, x_m. The length scale, x_m, is computed as the product of the timescale from Eq. 6, the velocity scale, U_∞, and a factor of 10 to account for the ten metastable lifetimes that are recorded as $x_m \approx 10\tau_m U_\infty$.

We note that in Table 1, the estimated lifetime of the metastable tracer is approximately the same for AEDC Tunnel 9 and the Mach 3 AEDC Calibration Tunnel with the orifice plates. This means that experiments in the Mach 3 AEDC Calibration Tunnel are a good simulation of future Tunnel 9 experiments. For longer-term goals, we plan to use KTV to measure the velocity profiles over flight vehicle
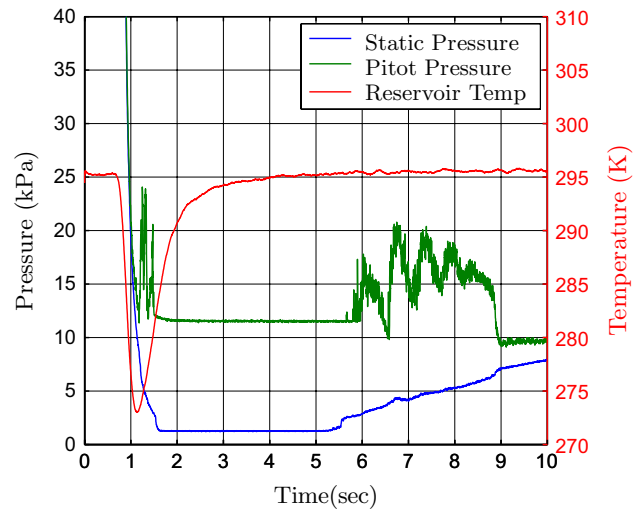

Fig. 4 Measurements of the static pressure, Pitot pressure, and reservoir temperature for the Mach 3 AEDC calibration tunnel with the 19.1 mm orifice plate. The steady test time is approximately 3 s, between 2 and 5 s

models in AEDC Tunnel 9 and high-enthalpy impulse facilities like Caltech's T5 reflected shock tunnel (Hornung 1993). The useful length scale for each of these facilities was derived from data in Marineau et al. (2015) (Tunnel 9) and Parziale et al. (2015b) (T5). In Table 1, it is seen that the metastable lifetime (τ_m) and the displacement distance (x_m) are estimated to be sufficient as to permit KTV measurements in Tunnel 9 or T5.

5 Krypton gas bottle cost and effect on transport properties

Krypton gas bottle cost is appropriate for laboratory-scale KTV efforts. In this work, we performed approximately ≈ 100 experiments with approximately ≈4k USD worth of premixed research grade 99 % N₂/1 % Kr gas, yielding a

≈40 USD per experiment cost. We initially estimated that the seeding cost per run of 1 % Kr mole fraction ranges from ≈10 USD in impulse facilities (e.g, Ludwieg Tubes, shocktunnels, and moderate reservoir pressure blow-down facilities) to ≈50–500 USD in high reservoir pressure long-duration blow-down hypersonic tunnels [e.g., Tunnel 9 at AEDC White Oak (Marren and Lafferty 2002)]. The range of cost is dependent on the unit Reynolds number of the windtunnel through local number density. For the Tunnel 9 condition listed in Table 1 ($Re_\infty^{\text{unit}} = 15e6$ 1/m), the estimated cost is ≈200 USD which is a small fraction of large-scale tunnel operation costs.

The thermo-physical properties of the N_2 flow are nominally unchanged with Kr seeding. Calculation of the effect of dilute krypton concentrations on the transport properties can be performed using Cantera (Goodwin 2003) via the semiempirical Chapman–Enskog method with the appropriate thermodynamic data (McBride et al. 2002). For example, if N_2 is seeded with 1 % Kr mole fraction at 300 K and 1 atm, the Reynolds, Prandtl, Lewis, and Peclet numbers, and the ratio of specific heats are changed by ≈0.1–0.3 %.

6 Supersonic turbulent boundary layer results

In this section, we present KTV- and Pitot-derived velocity profiles of the turbulent boundary layer on the wall of the AEDC White Oak Mach 3 Calibration Tunnel. The freestream was comprised of 99 % N_2/1 % Kr. The momentum thickness is defined as

$$\Theta = \int_0^\infty \frac{\rho}{\rho_e} \frac{U}{U_e} \left(1 - \frac{U}{U_e}\right) dy. \tag{7}$$

Using the KTV-derived velocity profiles, the momentum-thickness Reynolds numbers are determined to be $Re_\Theta = \rho_e U_e \Theta / \mu_e = 800, 1400$, and 2400. The momentum-thickness Reynolds numbers computed with the Pitot-derived velocity profiles result in the same values to within ≈3 %.

Pitot-derived velocity profiles were made at discrete wall-normal distances with Pitot and static pressure measurement using the same methodology as Brooks et al. (2014, 2015, 2016). The Mach number was found with the Rayleigh–Pitot probe formula (Eq. 4). The local temperature was found using the relation from Walz (1959),

$$\frac{T}{T_e} = \frac{T_w}{T_e} + \frac{T_r - T_w}{T_e} \left(\frac{U}{U_e}\right) - r \frac{\gamma - 1}{2} M_e^2 \left(\frac{U}{U_e}\right)^2, \tag{8}$$

with the recovery temperature, T_r, is defined as

$$\frac{T_r}{T_e} = 1 + r \frac{\gamma - 1}{2} M_e^2. \tag{9}$$

KTV measurements were performed by tracking the tagged Kr center-of-mass locations for a prescribed time. To find the local streamwise velocity, each exposure is processed with a 3 pixel × 3 pixel (≈291 μm × 291 μm) two-dimensional Wiener adaptive-noise removal filter in MAT-LAB. Example exposures that illustrate the unsteady nature of the supersonic turbulent boundary layer are presented as Fig. 5. For the $Re_\Theta = 800, 1400$, and 2400 cases, 425, 456, and 250 exposures are collected, respectively. A Gaussian model of the form $f(x) = a \exp\left(-((x - b)/c)^2\right)$ is fitted to the intensity vector for each exposure in the streamwise (x) direction for each row of pixels in the wall-normal (y) direction (≈97 μm wall-normal direction ×5.0 mm streamwise direction). The centroid (b) and the 95 % confidence bounds of the Gaussian fits are determined with the non-linear least-squares method. The streamwise displacement distance, Δx, is then found as the read-centroid location relative to the write-centroid location. The local velocity is found as $U = \Delta x / \Delta t$, where Δt is prescribed by a pulse/delay generator as $\Delta t = 2$ μs.

Examples of five representative rows of data for the write and read Kr line from the freestream are shown in Fig. 6. The data are recorded at separate times and superposed for presentation. In addition, the FWHM of 350 μm are shown as horizontal black bars for the write and read lines.

We present the dimensional velocity profiles for three conditions with $Re_\Theta = 800$ (Fig. 7), $Re_\Theta = 1400$ (Fig. 8), and $Re_\Theta = 2400$ (Fig. 9). The KTV results are reported along with Pitot tube-derived velocity measurements and predicted turbulent profiles from the Virginia Tech (VT) Compressible Turbulent Boundary Layer applet from Devenport and Schetz (1998, 1999), Shetz and Bowersox 2000).

For each case, $Re_\Theta = 800, 1400, 2400$, agreement between the three mean velocity profiles (KTV, Pitot, and VT Applet) is good, particularly between the Pitot and KTV measurements. The small discrepancy between the VT applet and the measurements may be because it is assumed that there is no pressure history (flat plate) and the transition occurs at the nozzle throat in the VT Applet calculations. Boundary layer trips were placed in the subsonic region near the nozzle throat which were characterized by an $Re_{kk} = \rho_* u_* k / \mu_* > 1000$, where * refers to the condition at the nozzle throat and k is the trip height (Reda 2002). However, particularly for the $Re_\Theta = 800$ case, the Reynolds number may not be sufficient to result in an equilibrium turbulent boundary layer at the measurement location which was ≈530 mm from the throat. The boundary layer trips were four forward- and backward-facing steps made of strips of adhesive tape spanning the width of the windtunnel. Each strip was ≈2.5 mm in width in the streamwise direction, separated by ≈5 mm, and ≈2 mm in height.

KTV results near the windtunnel wall ($y/\delta < 0.1$) are not reported because the Gaussian fits to the read data were
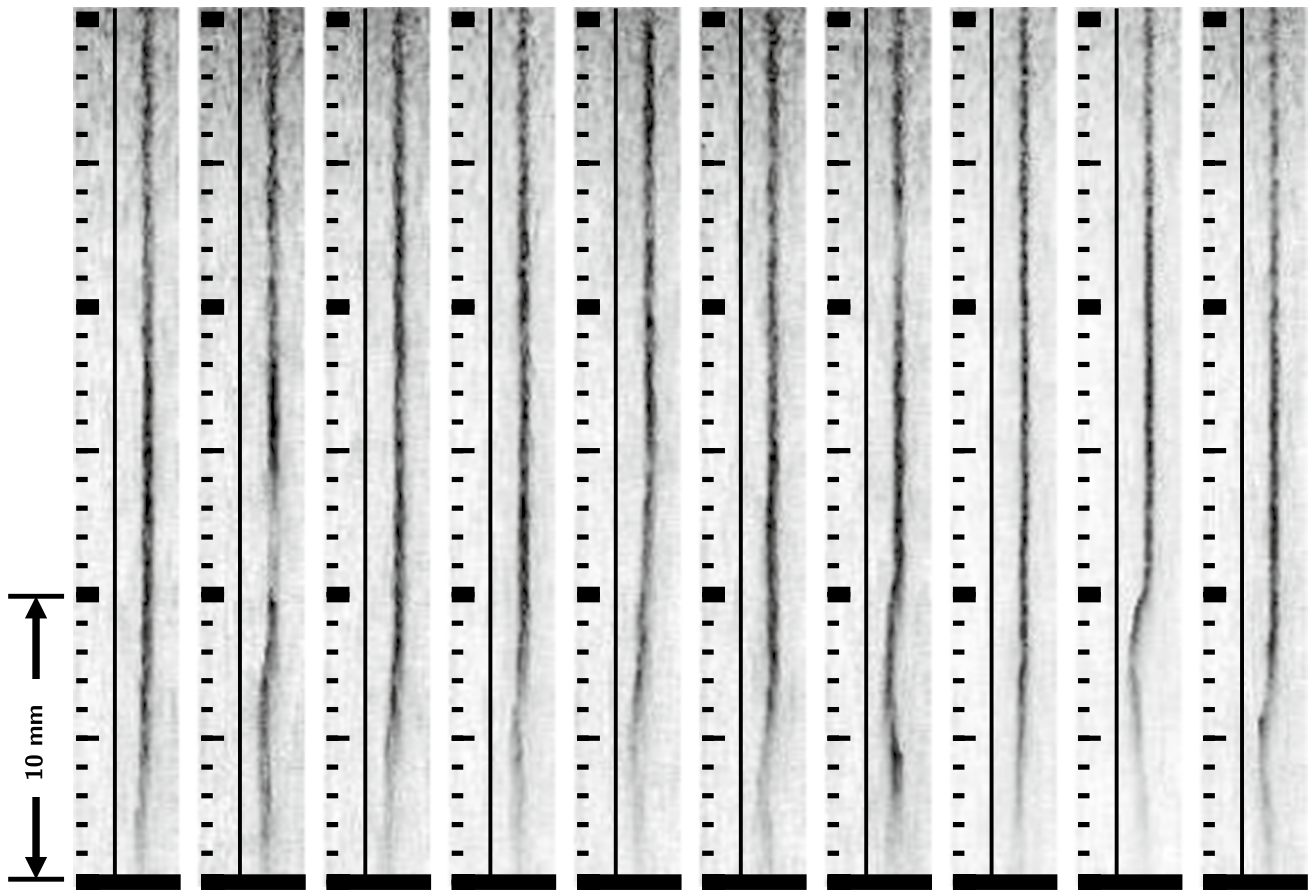
Fig. 5 KTV in a 99 % N_2/1 % Kr Mach 2.75 turbulent boundary layer with a $Re_\Theta = 800$. Flow is *left to right*. Inverted intensity scale. The write location is marked by a *vertical*, *thin black line*. The camera gate is fixed to include only the read-laser pulses. The delay between the write and read pulses is 2 µs. Major tick marks at 10 mm intervals, with label on *left*
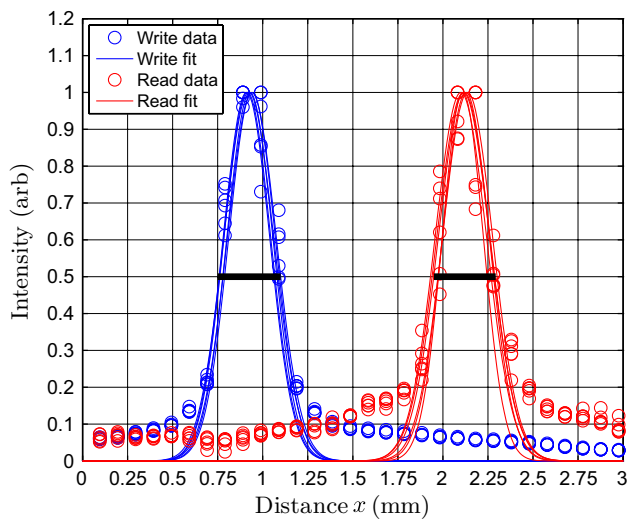

Fig. 6 Examples of write and read data from the freestream superposed to show displacement measurement by Gaussian fitting. In addition, 350 µm *black bars* mark the FWHM of the write and read intensity data
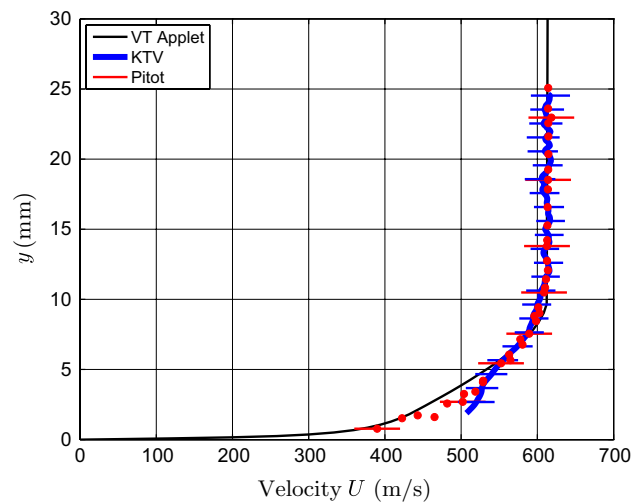
Fig. 7 Velocity profile in a 99 % N_2/1 % Kr Mach 2.75 turbulent boundary layer with $Re_\Theta = 800$. *Horizontal lines are error bars*

found to be unreliable; that is, the 95 % confidence bounds on the x-location of the read-line were found to be larger than the tracer width. The lack of repeatable results close to the windtunnel wall ($y/\delta < 0.1$) is likely due to the high levels of fluctuation which smear the KTV tracer, resulting in low SNR. Further study is required to confirm this.

Uncertainty in the velocimetry data was estimated following Moffat (1982). For the Pitot-derived velocity data, we assume that the uncertainty is determined by the Pitot pressure, static pressure, and reservoir temperature as

$$\delta U_{\text{Pitot}} = \left[\left(\delta P_{02}\frac{\partial U}{\partial P_{02}}\right)^2 + \left(\delta P_\infty \frac{\partial U}{\partial P_\infty}\right)^2 + \left(\delta T_\infty \frac{\partial U}{\partial T_\infty}\right)^2\right]^{\frac{1}{2}}. \quad (10)$$

The uncertainty in Pitot-derived velocity from the Pitot pressure and static pressure can be determined using the Rayleigh–Pitot probe formula (Eq. 4). The uncertainty in the pressure transducer response is from comparisons of in-house calibrations against high-accuracy Baratron pressure transducers. The uncertainty in Pitot-derived velocity from the reservoir temperature is determined using the sound speed, the isentropic gas relations to relate reservoir and static temperature, and the measured unsteadiness during the test time (Fig. 4). The vertical resolution of the Pitot probes is 800 μm, as reported in Brooks et al. (2015).

For the KTV-derived velocity data, we assume that the uncertainty is determined by the uncertainty in the measured displacement distance of the metastable tracer, the timing accuracy of the experiment, and the wall-normal motion of the metastable tracer in the xy-plane as
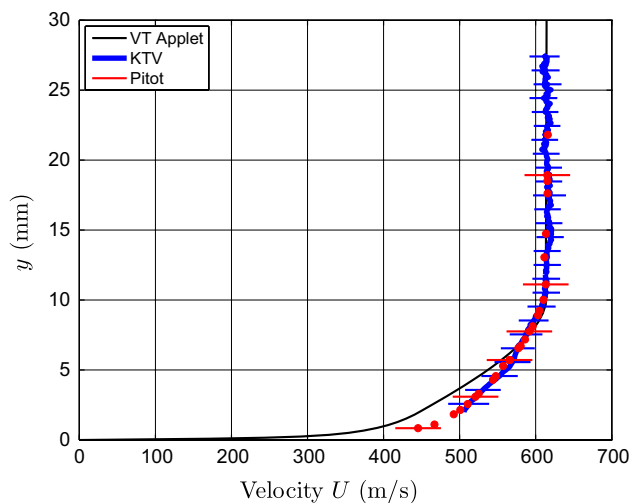

Fig. 8 Velocity profile in a 99 % N_2/1 % Kr Mach 2.77 turbulent boundary layer with $Re_\Theta = 1400$. *Horizontal lines* are *error bars*
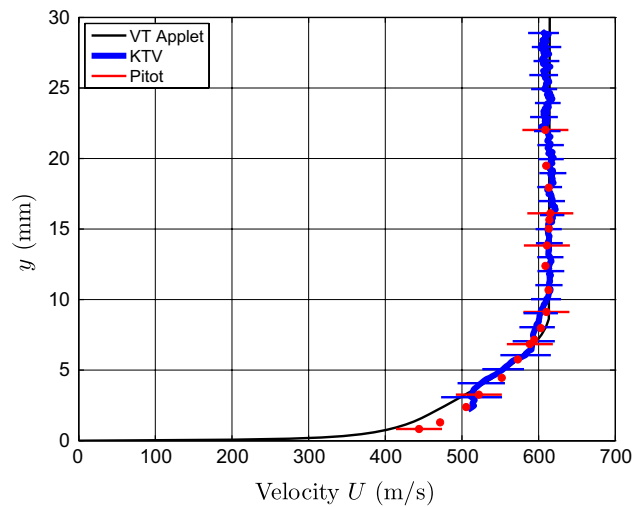

Fig. 9 Velocity profile in a 99 % N_2/1 % Kr Mach 2.73 turbulent boundary layer with $Re_\Theta = 2400$. *Horizontal lines* are *error bars*

$$\delta U_{\text{KTV}} = \left[\left(\delta \Delta x \frac{\partial U}{\partial \Delta x}\right)^2 + \left(\delta \Delta t \frac{\partial U}{\partial \Delta t}\right)^2 + \delta U_{IP}^2\right]^{\frac{1}{2}}. \quad (11)$$

The uncertainty in the measured displacement distance, Δx, of the metastable tracer is estimated as the 95 % confidence bound on the write and read locations from the nonlinear least-squares Gaussian fits. The uncertainty Δt is estimated to be 50 ns, primarily due to fluorescence blurring as considered in Bathel et al. (2011). From the manufacturers specification, we estimate that the timing jitter is relatively small, approximately 1 ns for each laser. The fluorescence blurring primarily occurs because of the time scale associated with the 819.0 nm $5p[3/2]_2 \rightarrow 5s[3/2]_1^o$ transition, which is approximately 25 ns (Chang et al. 1980; Whitehead et al. 1995; Dzierega et al. 2000); so, we double this value and report that as the uncertainty in Δt. The uncertainty in streamwise velocity due to wall-normal fluctuations in the xy-plane is estimated to be $\delta U_{IP} = v'_{\text{RMS}}(dU/dy)\Delta t$. This formulation is taken from Hill and Klewicki (1996) and Bathel et al. (2011). The wall-normal fluctuations, v'_{RMS}, are conservatively estimated to be 4 % of the edge velocity, which is supported by DNS (Martin 2007) and PIV experiments (Brooks et al. 2016).

Uncertainty estimates of the velocity profiles in Figs. 7, 8, and 9 appear as horizontal lines.

7 Analysis

In this section, the velocity profiles in Figs. 7, 8, and 9 are non-dimensionalized to analyze the KTV and Pitot data in the logarithmic and outer region of the boundary layer. The

shear velocity, $u_\tau = \sqrt{\tau_w/\rho_w}$, is required and the method of calculation can be found from Eq. 20 in Appendix.

The velocity data from the present study can be compared to the law of the wall in the logarithmic region, $U^+ = \frac{1}{\kappa}\ln(y^+) + C$, by using the Van Driest I transformation, with $y^+ = \rho_w u_\tau y/\mu_w$ and $U^+ = U/u_\tau$. Following Bradshaw (1977) and Huang and Coleman (1994), the Van Driest transformed velocity is written as

$$U_{VD}^+ = \frac{1}{R}\left[\sin^{-1}\left(\frac{R(U^+ + H)}{\sqrt{1 + R^2 H^2}}\right) - \sin^{-1}\left(\frac{RH}{\sqrt{1 + R^2 H^2}}\right)\right], \quad (12)$$

where $R = M_\tau\sqrt{(\gamma - 1)\Pr_t/2}$, $H = B_q/((\gamma - 1)M_\tau^2)$, $M_\tau = u_\tau/c_w$, and $B_q = q_w/(\rho_w c_p u_\tau T_w)$. We assume the turbulent Prandtl number is $\Pr_t = 0.87$, and, assuming the Reynolds analogy holds, the heat flux number is $B_q = c_f \rho_e U_e(T_w - T_r)/(2\Pr_e \rho_w u_\tau T_w)$ (Schlichting 2000). The turbulence Mach number and heat flux numbers are tabulated in Table 1. The transformed KTV- and Pitot-derived velocity profiles are presented in Fig. 10. Also, in Fig. 10, we plot the viscous sublayer as $U_{VD}^+ = y^+$ as well as applying Eq. 12 to the logarithmic law as

$$U_{VD}^+ = \frac{1}{\kappa}\ln(y^+) + C \quad (13)$$

with $\kappa = 0.41$ and $C = 5.2$. The transformed velocity follows the law of the wall in the logarithmic region with good agreement.

Coles (1956, 1962) proposed a modification of Eq. 13 to scale the outer region of the boundary layer known as the law of the wake. Using this scaling, Lewis et al. (1972) followed Coles (1956, 1962) and used

$$U_{VD}^+ = \frac{1}{\kappa}\ln(y^+) + C + \frac{2\Pi}{\kappa}\sin^2\left(\frac{\pi}{2}\frac{y}{\delta}\right) \quad (14)$$

and determined the boundary-layer thickness, δ, in a least-square-means sense to find the wake-strength parameter, $2\Pi/\kappa$. This is the procedure used here, and the wake-strength parameters and boundary layer thicknesses are reported in Table 1 for each case. The reduced velocity data is shown in Fig. 11. To better assess the scaling, an offset of 3 and 6 is added to the ordinate (C in Eq. 14) for the $Re_\Theta = 1400$ and 2400 cases, respectively. The wake-strength of the data increases with Reynolds number; this trend is consistent with the data from Coles (1956, 1962) and Lewis et al. (1972).

Fernholtz and Finley (1977, 1980) outline a velocity-defect law to scale the outer layer of the turbulent boundary layer. In their work, Fernholtz and Finley define an integral length scale

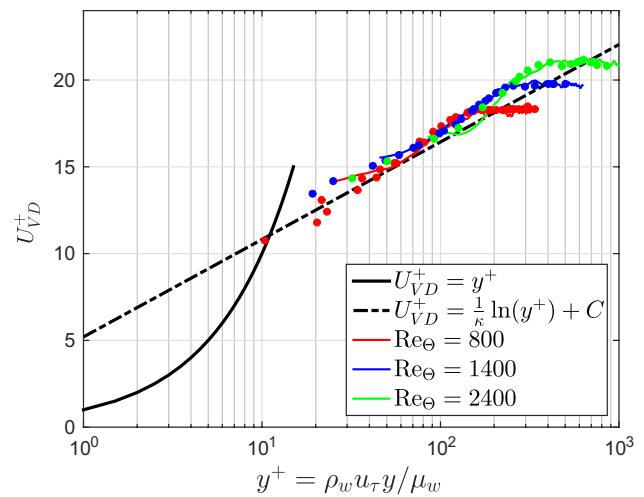$$\Delta^* = \int_0^\infty \frac{U_e^* - \bar{U}^*}{u_\tau}dy \quad (15)$$

Fig. 10 Van Driest transformed velocity compared to the law of the wall in the logarithmic region. Profiles in a 99 % N$_2$/1 % Kr Mach 2.7 turbulent boundary layer with $Re_\Theta = 800$, 1400, and 2400. *Dots* are Pitot-derived velocity. *Lines* are KTV-derived velocity

where U_e^* and $\bar{U}^*$ are the edge and local mean velocities defined by

$$U^* = \frac{U_e}{b}\sin^{-1}\frac{2b^2 U/U_e - a}{\sqrt{a^2 + 4b^2}} \quad (16)$$

and a and b are defined as

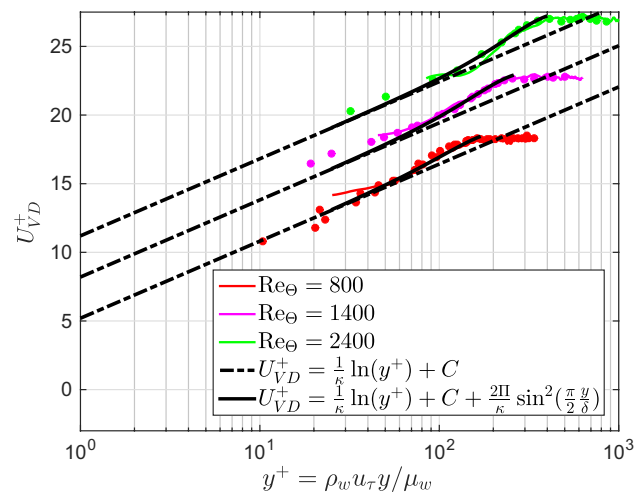$$a = \frac{T_e}{T_w}\left(1 + r\frac{\gamma - 1}{2}M_e^2\right) - 1 \quad (17)$$

Fig. 11 Van Driest transformed velocity compared to the law of the wake. Profiles in a 99 % N$_2$/1 % Kr Mach 2.7 turbulent boundary layer with $Re_\Theta = 800$, 1400, and 2400. *Dots* are Pitot-derived velocity. *Lines* are KTV-derived velocity. Offset of 3 and 6 added to ordinate (C in Eq. 14) for the $Re_\Theta = 1400$ and 2400 cases, respectively

$$b^2 = \frac{T_e}{T_w}\left(r\frac{\gamma-1}{2}M_e^2\right). \qquad (18)$$

The resulting non-dimensional profiles are presented as Fig. 12. Also in Fig. 12, we plot the velocity-defect law proposed by Fernholtz and Finley (1977, 1980),

$$\frac{U_e^* - \bar{U}^*}{u_\tau} = -M\ln\left(\frac{y}{\Delta^*}\right) - N, \qquad (19)$$

with $M = 4.7$ and $N = 6.74$. Here, M is not the Mach number but a constant that is consistent with the nomenclature of Fernholtz and Finley (1977, 1980). The proposed relation is for a turbulent boundary layer with zero pressure gradient. The agreement between the transformed KTV and Pitot velocity data and the velocity-defect law is poor. Fernholtz and Finley (1977, 1980) note that a deviation from this defect law may be due to Mach number, pressure gradients, or Reynolds number.

The RMS streamwise velocity fluctuations, $u'_{\rm rms}$, as measured by KTV and non-dimensionalized by the edge velocity are presented in Fig. 13. The KTV fluctuation measurements collapse for each case, except for the $Re_\Theta = 800$ case outside of the boundary layer. The reason for this raised level of fluctuation outside the boundary layer is unknown at the time of this writing.

The Morkovin (1962) scaling of the fluctuations ($\sqrt{\rho}u'_{\rm rms}/\sqrt{\rho_w}u_\tau$) is applied to the data and presented in Fig. 14. In that figure, we overlay data from the literature from hot-wire anemometry (HWA) measurements from Klebanoff (1955) recorded in a low-speed boundary layer (30 ft/s), and HWA and one- and two-component LDV measurements in a $M_e = 2.3, Re_\Theta = 4700$ boundary layer from Elena et al. (1985). We also overlay fluctuation data from PIV in the AEDC White Oak Mach 3 Calibration Tunnel from Brooks et al. (2016) which was recorded at the same tunnel location as the current KTV experiments at $Re_\Theta = 1740$ and $Re_\Theta = 2600$. These data are compared to direct numerical simulation (DNS) data in a $M_e = 2.3, Re_\Theta = 4450$ boundary layer from Martin (2007). The agreement between the KTV data from this work and the experimental and computational data is good for wall-normal distances $y/\delta > 0.2$.

8 Conclusions and future work

To assess the potential use of the KTV technique in AEDC Hypervelocity Tunnel 9, the Mach 3 AEDC Calibration Tunnel was modified so that the unit Reynolds number could be prescribed at several values consistent with AEDC Tunnel 9 run conditions. The modification was comprised of an orifice plate, PVC pipe, and three perforated screens. These components were successfully used to reduce the
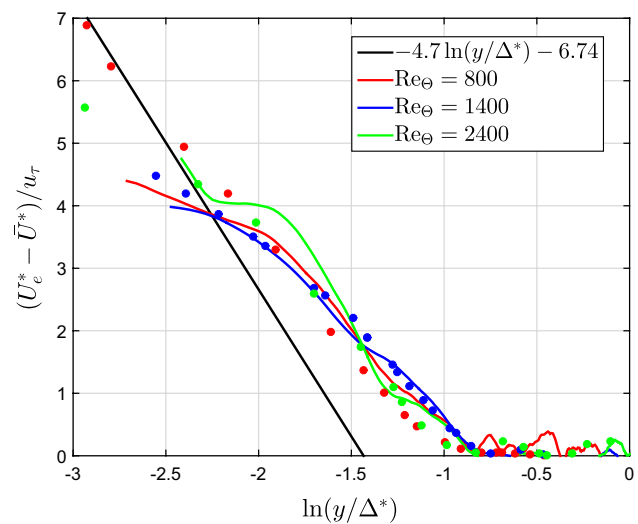
Fig. 12 Velocity-defect law scaling of velocimetry data for profiles in a 99 % N_2/1% Kr Mach 2.7 turbulent boundary layer with $Re_\Theta = 800, 1400, 2400$. *Dots* are Pitot-derived velocity. *Lines* are KTV-derived velocity
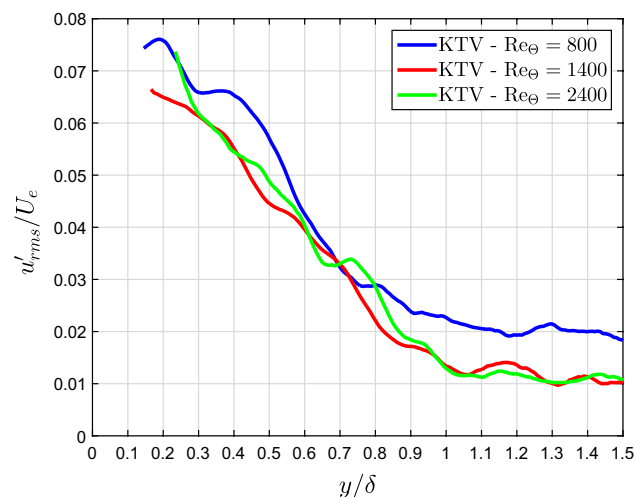

Fig. 13 Streamwise velocity fluctuation KTV data non-dimensionalized by the edge velocity

reservoir pressure, and thus the freestream unit Reynolds number.

In this work, we highlight the KTV measurement of a 99 % N_2/1 % Kr Mach 2.7 turbulent boundary layer at momentum-thickness Reynolds numbers of $Re_\Theta = 800$, 1400, and 2400. Pitot-derived velocity data were also taken for the flowfield, and agreement between the KTV- and Pitot-derived velocity profiles is excellent. Moreover, there is fair agreement between the experimental profiles of velocity (KTV and Pitot) with the predicted profiles from the Virginia Tech Compressible Turbulent Boundary Layer
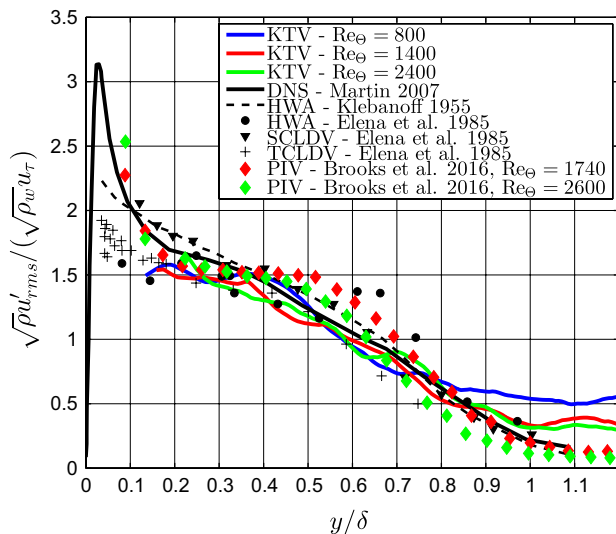
Fig. 14 Streamwise velocity fluctuation KTV data non-dimensionalized by the Morkovin scaling, and compared to historical data from Klebanoff ([1955](#)) from a low-speed tunnel, Elena et al. ([1985](#)) from a $M_e = 2.3$, $Re_\Theta = 4700$ boundary layer by HWA and one- and two-component LVD. Additionally, PIV measurements from Brooks et al. ([2016](#)) are presented. These data are compared to DNS from Martin ([2007](#)) from a $M_e = 2.3$, $Re_\Theta = 4450$ boundary layer

applet from Devenport and Schetz ([1998](#), [1999](#)); Shetz and Bowersox ([2000](#)).

The KTV- and Pitot-derived profiles of velocity are compared to the law of the wall with the application of the Van Driest I transformation, and agreement in the logarithmic region is good. From this, we conclude that KTV may be used to measure profiles of velocity in the logarithmic region of supersonic turbulent boundary layers.

In addition, a wake-strength parameter is fitted to the data with the boundary layer thickness, δ, as the free parameter. The wake-strength of the data increases with Reynolds number; this trend is consistent with the data from Coles ([1956](#), [1962](#)) and Lewis et al. ([1972](#)).

The data are also scaled according to the velocity-defect law outlined in Fernholtz and Finley ([1977](#), [1980](#)), and the KTV and Pitot profiles collapse for the data taken at $Re_\Theta = 800$, 1400 and 2400. The KTV and Pitot data do not closely follow the scaling reported by Fernholtz and Finley of $(U_e^* - \bar{U}^*)/(u_\tau) = -4.7 \log(y/\Delta^*) - 6.74$. Near the abscissa of Fig. [12](#), in the wake region, the present data fall $\ln(y/\Delta^+) > 1.5$. The deviation from the scaling of the data from the present work to the velocity-defect law may be due to the low Reynolds number or the favorable pressure gradient history from the nozzle expansion.

The KTV technique is used to quantify the streamwise velocity fluctuations. The KTV fluctuation measurements collapse for each case, except for the $Re_\Theta = 800$ case outside of the boundary layer. The reason for this raised level

of fluctuation outside the boundary layer is not clear at the time of this writing. The Morkovin scaling is applied to the RMS fluctuation data. The agreement between the computational and experimental data from the literature and KTV measurements from this work is good for wall-normal distances $y/\delta > 0.2$.

Measurements below $y/\delta \approx 0.1$–0.2 are difficult to perform with tagging velocimetry, and the issue in doing so with KTV in this application may be that the tracer is smeared out because of the increase in velocity fluctuations near the wall (Fig. [14](#)). In the future, it may be possible to resolve the near-wall fluctuations by reducing the time between the write- and read-laser pulses so as to reduce the turbulent diffusion of the metastable Kr tracer.

The KTV data presented in this paper are florescence exposures captured at 10 Hz. The Nd:YAG pump lasers and the intensified camera used to perform the work set this 10 Hz limitation. That is, there is no fundamental physical principal of the KTV excitation/emission scheme that would preclude a significant increase in the rate at which exposures may be captured other than the delay between the write- and read-laser pulses. Advances in CMOS cameras, image intensifiers, and the development of pulsed burst lasers (Lempert et al. [1996](#); Wu et al. [2000](#)) could yield a setup that captures KTV exposures at a higher rate. High-repetition rate ultrafast lasers have also been developed, and could be particularly suitable for the initial multi-photon excitation of the Kr atoms. This is because, in comparison with single-photon excitations, multi-photon excitations are significantly more sensitive to pulse intensity (Denk et al. [1990](#)).

In addition, future experiments are planned which include attempting to probe the flow about geometries more complex than a windtunnel wall. Because more complex geometries may not be made of glass, a masking strategy will have to be devised to limit or eliminate damage to the model. Preliminary efforts toward this end have been successful with absorptive tape. Additionally, future experiments are planned where the legacy dye lasers in the current experimental setup are replaced with modern dye lasers and/or optical parametric oscillators (OPOs) for wavelength tuning. This would increase the available pulse energy which would enable an increase of SNR and the writing of multiple lines or grids. This may enable data collection closer to the wall and/or collection of two-dimensional tagging velocimetry data.

Appendix: Calculation of skin friction and shear velocity

To determine the shear velocity, $u_\tau = \sqrt{\tau_w/\rho_w}$, the shear stress at the wall, τ_w, must be determined. Following Xu and Martin (2004), the skin friction coefficient, $c_f = \tau_w/(0.5\rho_e U_e^2)$, can be determined from the von Kármán (1934)-Schoenherr (1932) equation under the Van Driest II transformation as

$$\frac{1}{c_f F_c} = 17.08 \big(\log_{10}(F_\Theta \mathrm{Re}_\Theta)\big)^2$$
$$+ 25.11 \log_{10}(F_\Theta \mathrm{Re}_\Theta) + 6.012 \tag{20}$$

where

$$F_c = 0.2 r M_e^2/(\sin^{-1}(\alpha) + \sin^{-1}(\beta))^2, \tag{21}$$

$$F_\Theta = \mu_e/\mu_w, \tag{22}$$

and $r = 0.9$ is the recovery factor. The parameters α and β are computed as

$$\alpha = (2A^2 - B)/\sqrt{4A^2 + B^2} \tag{23}$$

$$\beta = B/\sqrt{4A^2 + B^2} \tag{24}$$

with

$$A^2 = 0.2 r M_e^2/(T_w/T_e) \tag{25}$$

$$B = (1 + 0.2 r M_e^2 - T_w/T_e)/(T_w/T_e). \tag{26}$$

References

Balla RJ (2013) Iodine tagging velocimetry in a Mach 10 wake. AIAA J 51(7):1–3. doi:10.2514/1.J052416

Balla RJ, Everhart JL (2012) Rayleigh scattering density measurements, cluster theory, and nucleation calculations at Mach 10. AIAA J 50(3):698–707. doi:10.2514/1.J051334

Bathel BF, Danehy PM, Inman JA, Jones SB, Ivey CB, Goyne CP (2011) Velocity profile measurements in hypersonic flows using sequentially imaged fluorescence-based molecular tagging. AIAA J 49(9):1883–1896. doi:10.2514/1.J050722

Bilardo VJ, Curran FM, Hunt JL, Lovell NT, Maggio G, Wilhite AW, McKinney LE (2003) The benefits of hypersonic airbreathing launch systems for access to space. In: Proceedings of 39TH AIAA/ASME/SAE/ASEE joint propulsion conference and exhibit, AIAA-2003-5265, Huntsville, Alabama. doi:10.2514/6.2003-5265

Boedeker LR (1989) Velocity measurement by H_2O photolysis and laser-induced fluorescence of OH. Opt Lett 14(10):473–475. doi:10.1364/OL.14.000473

Bose D, Brown JL, Prabhu DK, Gnoffo P, Johnston CO, Hollis B (2013) Uncertainty assessment of hypersonic aerothermodynamics prediction capability. J Spacecr Rockets 50(1):12–18. doi:10.2514/1.A32268

Bradshaw P (1977) Compressible turbulent shear layers. Annu Rev Fluid Mech 9(1):33–52. doi:10.1146/annurev.fl.09.010177.000341

Brooks J, Gupta A, Smith MS, Marineau EC (2014) Development of non-intrusive velocity measurement capabilities at AEDC Tunnel 9. In: Proceedings of 52nd aerospace sciences meeting, SciTech, AIAA-2014-1239, National Harbor, Maryland. doi:10.2514/6.2014-1239

Brooks JM, Gupta AK, Smith MS, Marineau EC (2015) Development of particle image velocimetry in a Mach 2.7 Wind Tunnel at AEDC White Oak. In: Proceedings of 53nd aerospace sciences meeting, SciTech, AIAA-2015-1915, Kissimmee, Florida. doi:10.2514/6.2015-1915

Brooks JM, Gupta AK, Smith MS, Marineau EC (2016) PIV measurements of Mach 2.7 turbulent boundary layer with varying Reynolds numbers. In: Proceedings of 54th aerospace sciences meeting, SciTech, AIAA-2016-1147, San Diego, California. doi:10.2514/6.2016-1147

Candler GV (2015) Rate-dependent energetic processes in hypersonic flows. Prog Aerosp Sci 72:37–48. doi:10.1016/j.paerosci.2014.09.006

Chang RSF, Horiguchi H, Setser DW (1980) Radiative lifetimes and two-body collisional deactivation rate constants in argon for Kr (4 p ^{5}5 p) and Kr (4 p ^{5}5 p) states. J Chem Phys 73(2):778–790. doi:10.1063/1.440185

Charonko JJ, King CV, Smith BL, Vlachos PP (2010) Assessment of pressure field calculations from particle image velocimetry measurements. Meas Sci Technol 21(10):105,401. doi:10.1088/0957-0233/21/10/105401

Clemens NT, Narayanaswamy V (2014) Low-frequency unsteadiness of shock wave/turbulent boundary layer interactions. Ann Rev Fluid Mech 46:469–492. doi:10.1146/annurev-fluid-010313-141346

Coles DE (1956) The law of the wake in the turbulent boundary layer. J Fluid Mech 1(2):191–226. doi:10.1017/S0022112056000135

Coles DE (1962) The turbulent boundary layer in a compressible fluid. RAND R-403-PR

Dam N, Klein-Douwel RJH, Sijtsema NM, ter Meulen JJ (2001) Nitric oxide flow tagging in unseeded air. Opt Lett 26(1):36–38. doi:10.1364/OL.26.000036

Denk W, Strickler JH, Webb WW (1990) Two-photon laser scanning fluorescence microscopy. Science 248(4951):73–76. doi:10.1126/science.2321027

Devenport WJ, Schetz JA (1998) Boundary layer codes for students in Java. In: Proceedings of the ASME fluids engineering division summer meeting, ASME, Washington, DC, FEDSM98-5139

Devenport WJ, Schetz JA (1999) Heat transfer codes for students in Java. In: Proceedings of the 5th ASME/JSME thermal engineering joint conference, ASME, San Diego, California, AJTE99-6229

Dzierega K, Volz U, Nave G, Griesmann U (2000) Accurate transition rates for the $5p$–$5s$ transitions in Kr I. Phys Rev A 62(2):022505. doi:10.1103/PhysRevA.62.022505

Eckbreth AC (1996) Laser diagnostics for combustion temperature and species, 2nd edn. Gordon and Breach Publications

Edwards MR, Dogariu A, Miles RB (2015) Simultaneous temperature and velocity measurements in air with femtosecond laser tagging. AIAA J 53(8):2280–2288. doi:10.2514/1.J053685

Elena M, Lacharme JP, Gaviglio J (1985) Comparison of hot-wire and laser Doppler anemometry methods in supersonic turbulent

boundary layers. In: Proceedings of 2nd international symposium on laser anemometry, Miami Beach, Florida, pp 151–157

Fernholtz HH, Finley PJ (1977) A critical compilation of compressible turbulent boundary layer data. AGARD-223

Fernholtz HH, Finley PJ (1980) A critical commentary on mean flow data for two-dimensional compressible turbulent boundary layers. AGARD-253

Gendrich CP, Koochesfahani MM (1996) A spatial correlation technique for estimating velocity fields using molecular tagging velocimetry (MTV). Exp Fluids 22(1):67–77. doi:10.1007/BF01893307

Gendrich CP, Koochesfahani MM, Nocera DG (1997) Molecular tagging velocimetry and other novel applications of a new phosphorescent supramolecule. Exp Fluids 23(5):361–372. doi:10.1007/s003480050123

Goodwin DG (2003) An open-source, extensible software suite for CVD process simulation. In: Allendorf M, Maury F, Teyssandier F (eds) Proceedings of CVD XVI and EuroCVD fourteen, pp 155–162

Haertig J, Havermann M, Rey C, George A (2002) Particle image velocimetry in Mach 3.5 and 4.5 shock-tunnel flows. AIAA J 40(6):1056–1060. doi:10.2514/2.1787

Handa T, Mii K, Sakurai T, Imamura K, Mizuta S, Ando Y (2014) Study on supersonic rectangular microjets using molecular tagging velocimetry. Exp Fluids 55(5):1–9. doi:10.1007/s00348-014-1725-5

Hill RB, Klewicki JC (1996) Data reduction methods for flow tagging velocity measurements. Exp Fluids 20(3):142–152. doi:10.1007/BF00190270

Hiller B, Booman RA, Hassa C, Hanson RK (1984) Velocity visualization in gas flows using laser-induced phosphorescence of biacetyl. Rev Sci Instrum 55(12):1964–1967. doi:10.1063/1.1137687

Hornung HG (1993) Experimental hypervelocity flow simulation, needs, achievements and limitations. In: Proceedings of the first pacific international conference on aerospace science and technology, Taiwan

Hsu AG, Srinivasan R, Bowersox RDW, North SW (2009a) Molecular tagging using vibrationally excited nitric oxide in an underexpanded jet flowfield. AIAA J 47(11):2597–2604. doi:10.2514/1.39998

Hsu AG, Srinivasan R, Bowersox RDW, North SW (2009b) Two-component molecular tagging velocimetry utilizing NO fluorescence lifetime and NO_2 photodissociation techniques in an underexpanded jet flowfield. Appl Opt 48(22):4414–4423. doi:10.1364/AO.48.004414

Huang PG, Coleman GN (1994) Van Driest transformation and compressible wall-bounded flows. AIAA J 32(10):2110–2113. doi:10.2514/3.12259

Klebanoff PS (1955) Characteristics of turbulence in a boundary layer with zero pressure gradient. NACA TR-1247

Lempert WR, Wu PF, Zhang B, Miles RB, Lowrance JL, Mastracola V, Kosonocky WF (1996) Pulse-burst laser system for high-speed flow diagnostics. In: Proceedings of 34th aerospace sciences meeting and exhibit, AIAA 1996-0179, Reno, Nevada. doi:10.2514/6.1996-179

Lempert WR, Jiang N, Sethuram S, Samimy M (2002) Molecular tagging velocimetry measurements in supersonic microjets. AIAA J 40(6):1065–1070. doi:10.2514/2.1789

Lempert WR, Boehm M, Jiang N, Gimelshein S, Levin D (2003) Comparison of molecular tagging velocimetry data and direct simulation monte carlo simulations in supersonic micro jet flows. Exp Fluids 34(3):403–411. doi:10.1007/s00348-002-0576-7

Lewis JE, Gran RL, Kubota T (1972) An experiment on the adiabatic compressible turbulent boundary layer in adverse and favourable pressure gradients. J Fluid Mech 51(4):657–672. doi:10.1017/S0022112072001296

Liepmann HW, Roshko A (1957) Elements of gasdynamics. Wiley, New York

Loth E (2008) Compressibility and rarefaction effects on drag of a spherical particle. AIAA J 46(9):2219–2228. doi:10.2514/1.28943

Marineau EC, Moraru GC, Lewis DR, Norris JD, Lafferty JD, Johnson HB (2015) Investigation of Mach 10 boundary layer stability of sharp cones at angle-of-attack, part 1: experiments. In: Proceedings of AIAA SciTech 2015, AIAA-2015-1737, Kissimmee, Florida. doi:10.2514/6.2015-1737

Marren D, Lewis M, Maurice LQ (2001) Experimentation, test, and evaluation requirements for future airbreathing hypersonic systems. J Propuls Power 17(6):1361–1365. doi:10.2514/2.5888

Marren D, Lafferty, J (2002) The AEDC hypervelocity wind Tunnel 9. In: Advanced hypersonic test facilities. American Institute of Aeronautics and Astronautics, pp 467–478. doi:10.2514/5.9781600866678.0467.0478

Martin MP (2007) Direct numerical simulation of hypersonic turbulent boundary layers. Part 1. Initialization and comparison with experiments. J Fluid Mech 570:347–364. doi:10.1017/S0022112006003107

McBride BJ, Zehe MJ, Gordon S (2002) NASA Glenn coefficients for calculating thermodynamic properties of individual species. NASA TP-2002-211556

McDaniel JC, Hiller B, Hanson RK (1983) Simultaneous multiple-point velocity measurements using laser-induced iodine fluorescence. Opt Let 8(1):51–53. doi:10.1364/OL.8.000051

McKeon B, Comte-Bellot G, Foss J, Westerweel J, Scarano F, Tropea C, Meyers J, Lee J, Cavone A, Schodl R, Koochesfahani M, Andreopoulos Y, Dahm W, Mullin J, Wallace J, Vukoslavevi P, Morris S, Pardyjak E, Cuerva A (2007) Velocity, vorticity, and Mach number. In: Tropea C, Yarin AL, Foss JF (eds) Springer handbook of experimental fluid mechanics. Springer, Berlin

Michael JB, Edwards MR, Dogariu A, Miles RB (2011) Femtosecond laser electronic excitation tagging for quantitative velocity imaging in air. Appl Opt 50(26):5158–5162. doi:10.1364/AO.50.005158

Miles R, Cohen C, Connors J, Howard P, Huang S, Markovitz E, Russell G (1987) Velocity measurements by vibrational tagging and fluorescent probing of oxygen. Opt Lett 12(11):861–863. doi:10.1364/OL.12.000861

Miles R, Connors J, Markovitz E, Howard P, Roth G (1989) Instantaneous profiles and turbulence statistics of supersonic free shear layers by Raman excitation plus laser-induced electronic fluorescence (RELIEF) velocity tagging of oxygen. Exp Fluids 8(1–2):17–24. doi:10.1007/BF00203060

Miles RB, Lempert WR (1997) Quantitative flow visualization in unseeded flows. Annu Rev Fluid Mech 29(1):285–326. doi:10.1146/annurev.fluid.29.1.285

Miles RB, Zhou D, Zhang B, Lempert WR (1993) Fundamental turbulence measurements by RELIEF flow tagging. AIAA J 31(3):447–452. doi:10.2514/3.11350

Miles RB, Grinstead J, Kohl RH, Diskin G (2000) The RELIEF flow tagging technique and its application in engine testing facilities and for helium–air mixing studies. Meas Sci Technol 11(9):1272–1281. doi:10.1088/0957-0233/11/9/304

Mills JL, Sukenik CI, Balla RJ (2011) Hypersonic wake diagnostics using laser induced fluorescence techniques. In: Proceedings of 42nd AIAA plasmadynamics and lasers conference, AIAA 2011-3459, Honolulu, Hawaii. doi:10.2514/6.2011-3459

Moffat RJ (1982) Contributions to the theory of single-sample uncertainty analysis. J Fluids Eng 104(2):250–258. doi:10.1115/1.3241818

Morkovin MV (1962) Effects of compressibility on turbulent flows. In: Favre AJ (ed) Mécanique de la Turbulence. CNRS, pp 367–380

Parziale NJ, Smith MS, Marineau EC (2015a) Krypton tagging velocimetry for use in high-speed ground-test facilities. In:

Proceedings of AIAA SciTech 2015, AIAA-2015-1484, Kissimmee, Florida. doi:10.2514/6.2015-1484

Parziale NJ, Smith MS, Marineau EC (2015b) Krypton tagging velocimetry of an underexpanded jet. Appl Opt 54(16):5094–5101. doi:10.1364/AO.54.005094

Pitz RW, Lahr MD, Douglas ZW, Wehrmeyer JA, Hu S, Carter CD, Hsu KY, Lum C, Koochesfahani MM (2005) Hydroxyl tagging velocimetry in a supersonic flow over a cavity. Appl Opt 44(31):6692–6700. doi:10.1364/AO.44.006692

Reda DC (2002) Review and synthesis of roughness-dominated transition correlations for reentry applications. J Spacecr Rockets 39(2):161–167. doi:10.2514/2.3803

Sánchez-González R, Srinivasan R, Bowersox RDW, North SW (2011) Simultaneous velocity and temperature measurements in gaseous flow fields using the venom technique. Opt Lett 36(2):196–198. doi:10.1364/OL.36.000196

Sánchez-González R, Bowersox RDW, North SW (2012) Simultaneous velocity and temperature measurements in gaseous flowfields using the vibrationally excited nitric oxide monitoring technique: a comprehensive study. Appl Opt 51(9):1216–1228. doi:10.1364/AO.51.001216

Sánchez-González R, Bowersox RDW, North SW (2014) Vibrationally excited NO tagging by NO ($A\,^2\Sigma^+$) fluorescence and quenching for simultaneous velocimetry and thermometry in gaseous flows. Opt Lett 39(9):2771–2774. doi:10.1364/OL.39.002771

Schlichting H (2000) Boundary-layer theory. Springer, Berlin

Schoenherr KE (1932) Resistance of flat surfaces moving through a fluid. Dissertation, Johns Hopkins University

Schwartzentruber TE, Boyd ID (2015) Progress and future prospects for particle-based simulation of hypersonic flow. Prog Aerosp Sci 72:66–79. doi:10.1016/j.paerosci.2014.09.003

Shetz JA, Bowersox RDW (2000) Boundary layer analysis. AIAA education series, 2nd edn. AIAA, Reston, VA

Sijtsema NM, Dam NJ, Klein-Douwel RJH, ter Meulen JJ (2002) Air photolysis and recombination tracking: a new molecular tagging velocimetry scheme. AIAA J 40(6):1061–1064. doi:10.2514/2.1788

Stier B, Koochesfahani MM (1999) Molecular tagging velocimetry (MTV) measurements in gas phase flows. Exp Fluids 26(4):297–304. doi:10.1007/s003480050292

Van der Laan WPN, Tolboom RAL, Dam NJ, ter Meulen JJ (2003) Molecular tagging velocimetry in the wake of an object in supersonic flow. Exp Fluids 34(4):531–534. doi:10.1007/s00348-003-0593-1

Velazco JE, Kolts JH, Setser DW (1978) Rate constants and quenching mechanisms for the metastable states of argon, krypton, and xenon. J Chem Phys 69(10):4357–4373. doi:10.1063/1.436447

von Kármán T (1934) Turbulence and skin friction. J Aeronaut Sci 1(1):1–20. doi:10.2514/8.5

Walz A (1959) Compressible turbulent boundary layers with heat transfer and pressure gradient in flow direction. J Res Natl Bur Stand B 63B(1):53–70. doi:10.6028/jres.063B.008

Wehrmeyer JA, Ribarov LA, Oguss DA, Pitz RW (1999) Flame flow tagging velocimetry with 193-nm H_2O photodissociation. Appl Opt 38(33):6912–6917. doi:10.1364/AO.38.006912

Whitehead CA, Pournasr H, Bruce MR, Cai H, Kohel J, Layne WB, Keto JW (1995) Deactivation of two-photon excited Xe($5p\,^56p,6p',7p$) and Kr ($4p\,^55p$) in xenon and krypton. J Chem Phys 102(5):1965–1980. doi:10.1063/1.468763

Woolf AF (2014) Conventional prompt global strike and long-range ballistic missiles: background and issues. Congressional Research Service R41464

Wu P, Lempert WL, Miles RB (2000) Megahertz pulse-burst laser and visualization of shock-wave/boundary-layer interaction. AIAA J 38(4):672–679. doi:10.2514/2.1009

Xu S, Martin MP (2004) Assessment of inflow boundary conditions for compressible turbulent boundary layers. Phys Fluids 16(7):2623–2639. doi:10.1063/1.1758218